Light Emitting Si-Based Mie Resonators: Toward a Huygens Source of Quantum Emitters

Mario Khoury, Hugo Quard, Tobias Herzig, Jan Meijer, Sébastien Pezzagna, Sébastien Cueff, Marco Abbarchi, Hai Son Nguyen, Nicolas Chauvin, Thomas Wood

ORIGINAL ARTICLE

Light emitting Si-based Mie resonators: towards a Huygens source of quantum emitters

Mario Khoury[1*] | Hugo Quard[2*] | Tobias Herzig[3] | Jan Meijer[3] | Sebastian Pezzagna[3] | Sebastien Cueff[2] | Marco Abbarchi[1,4] | Hai Son Nguyen[2,5] | Nicolas Chauvin[2] | Thomas Wood[2]

[1]Aix Marseille Univ, CNRS, Université de Toulon, IM2NP, UMR 7334, F-13397 Marseille, France

[2]Univ Lyon, Ecole Centrale de Lyon, INSA Lyon, Université Claude Bernard Lyon 1, CPE Lyon, CNRS, INL, UMR5270, Ecully 69130, France

[3]Division of Applied Quantum Systems, Felix-Bloch Institute for Solid-State Physics, University Leipzig, Linnéestrasse 5, 04103 Leipzig, Germany

[4]Solnil, 95 Rue de la République, 13002 Marseille, France

[5]IUF, Université de France

Correspondence
Email: marco.abbarchi@im2np.fr; thomas.wood@insa-lyon.fr

Funding information
This work was supported by the French National Research Agency (ANR) through the projects ULYSSES (No. ANR-15-CE24-0027-01) and OCTOPUS (No. ANR-18-CE47-0013-01), and the European Union's Horizon 2020 program through the FET-OPEN project NARCISO (No. 828890).

Silicon-based micro- and nano-structures for light management at near-infrared and visible frequencies have been widely exploited for guided optics and metasurfaces. However, light emission with this material has been hampered by the indirect character of its bandgap. Here we show that, via ion beam implant, light emitting G-centers can be directly embedded within Si-based Mie resonators previously obtained by solid state dewetting. Size- and position-dependent, directional light emission at 120 K is demonstrated experimentally and confirmed by Finite Difference Time Domain simulations. We estimate that, with an optimal coupling of the G-centers emission with the resonant antennas, a collection efficiency of about 90% can be reached using a conventional objective lens. The integration of these telecom-frequency emitters in resonant antennas is relevant for their efficient exploitation in quantum optics applications and more generally to Si-based photonic metasurfaces.

KEYWORDS
Mie resonators, light emitters in silicon, G-centers, telecom frequency

Abbreviations:

*Equally contributing authors.

1 | INTRODUCTION

Thanks to the transparency window and high permittivity of silicon, efficient optical devices have been implemented at near infrared frequencies for guided optics and integrated photonic circuits[1, 2]. Devices with relatively low Q-factors, such as dielectric Mie resonators, have been also used at shorter wavelengths for optical metasurfaces, structural color, anti-reflection coatings, quantum optics and much more[3, 4, 5].

The integration of light emitters in silicon however, has been limited by the indirect nature of its band-gap. Si-based, light-emitting metasurfaces [6] have been demonstrated using more or less complex fabrication methods, such as spin coating colloidal quantum dots[7], or by atomic layer deposition[8], deposition of organic molecules[9], or coupling an emitting 2D material with sub-micrometric antennas[10, 11, 12]. These approaches do not embed the emitters in the core of the resonators, where the the electromagnetic field is stronger and electric- and magnetic-dipolar Mie modes can be tailored, providing more versatility for light management[13, 14, 15, 16], as for instance shown for rare earth emitters coupled with plasmonic antennas[17] and light-emitting Si-nanocrystals in SiO_2 pillars[18]. Moreover, the presence of interfaces (e.g. produced by top-down lithographic methods) may be detrimental for the excitonic recombination owing to high concentrations of extrinsic defects. Epitaxial growth of Ge quantum dots is a viable alternative to embed light emitters within silicon-based photonic devices (e.g. at defined positions within the antennas[19] or in a photonic crystal[20]). However, these kind of emitters suffer from a relatively low quantum efficiency.

Complex impurities in silicon are well-known light emitters that can be easily created via standard ion implant methods or via high-energy electron beams[21, 22, 23, 24]. Very recently, they have been intensively investigated, especially in view of their exploitation as sources of single photons[25]. At low temperature ($\sim$10 K), their photoluminescence is composed of a sharp zero-phonon line (ZPL) and a low-energy phonon-side band covering a broad wavelength range[26, 27, 28, 29, 30, 31, 32, 33, 34]. Some of these impurities feature large quantum efficiency (e.g. of the order of unity[28]), relatively fast recombination lifetime (less than 10 ns[24]), large Debye-Waller factor (larger than 30%[29]) and a spin degree of freedom, offering a spin-photon interface[27, 34, 31]. In spite of their relevance in quantum optics, the integration of these emitters in photonic devices has been, so far, mostly limited to photonic crystals and photonic metasurfaces, requiring complex fabrication steps (e.g. e-beam lithography and reactive ion etching)[35, 36, 37]. First examples of integrated photonic circuits have been demonstrated very recently [38], accounting for the potential of point defects in Si.

We combine the features of dielectric, Si-based Mie resonators with light emitting impurities at telecom frequency, in order to obtain a directional light source and a large extraction efficiency. In analogy with the Kerker effect[13, 14, 15, 16], combining the resonant modes formed in the Si-based antennas (e.g. magnetic and electric dipolar modes) results in constructive and destructive interference that enhances or suppresses the scattering in specific directions, resulting in a strong light steering (analogous to with a Huygens-like light source). In order to achieve this result, we first integrate carbon-related impurities (G-centers) in self-assembled, atomically-smooth, Si-based sub-micrometric islands, acting as Mie resonators. We obtain these antennas by self-assembly via solid-state-dewetting: combining a top-down, low-resolution lithography step with a natural surface instability we produce atomically-smooth, monocrystalline and defect-free resonant antennas whose morphology is defined by the equilibrium shape of the Si crystal. We optimize 1) particle size providing resonant modes at the emitters' wavelength, 2) position (depth) of the emitters within the antennas to place them at the maximum of the electromagnetic field of the underlying Mie modes, and 3) proton fluence in order to maximise the number of light emitting G-centers. Spectroscopic investigation of the ensemble is systematically adopted to characterize the combined antenna-emitter system that appears highly sensitive to all of the structural parameters at play. By setting the optimal island size, emitter position and proton fluence, we demonstrate that the far-field emission pattern of the near-infrared photoluminescence from the G-centers can be reconstructed up to 120 K, accounting for the high quality of our samples. Furthermore, the optimal coupling of the G-centers with the antennas provides a directional emission in the far-field allowing for a collection efficiency as large as 90%

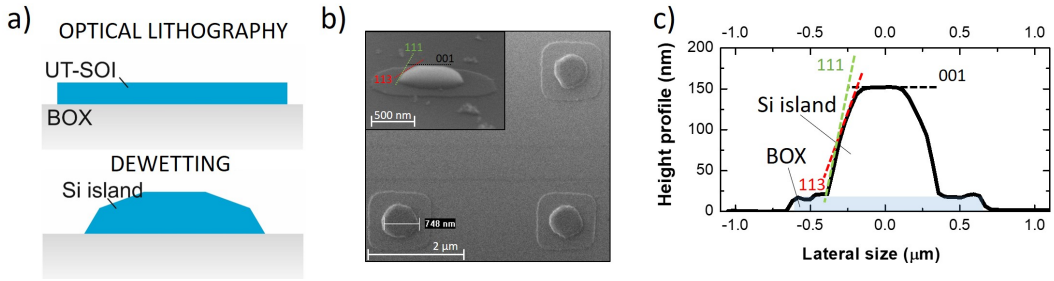

FIGURE 1 Sample fabrication. a) Optical lithography (top panel) is used to define $\sim \mu$m sized, square patches of ultra-thin silicon on insulator (UT-SOI) atop a thick SiO_2 buried oxide (BOX) of 2 μm. High temperature annealing (bottom panel) in ultra-high vacuum (about 10^{-10} torr) is used to induce the solid-state dewetting of the UT-SOI patches in 3D islands (for more details on the dewetting method see references [39, 40, 41]). b) Scanning electron microscope (SEM) image dewetted islands from an array of Si-islands obtained dewetting $\sim$1.5 μm wide patches. The top right inset shows a SEM tilted view at 70 degrees of a dewetted island. The main crystallographic axes of the equilibrium shape of Si are highlighted. For an extensive SEM characterization of similar samples obtained with the same method see reference [42]. c) Height profile of a Si island form the array shown in b) obtained from an atomic force microscope image. The BOX is highlighted with a shaded area. The facets typical of the equilibrium shape of Si are highlighted with dashed lines and labelled.

using conventional optics. These results are compared with Finite Difference Time Domain (FDTD) simulations accounting for the experimentally observed directional emission.

2 | RESULTS

2.1 | Sample fabrication

We first provide a description of the sample fabrication to create Si-based, sub-micrometric islands working as Mie resonators (Figure 1) and their activation with G-centers via ion implant (Figure 2).

Fabrication of Si resonant antennas via dewetting[39, 40, 41, 43] and the characterization of their optical properties under white light illumination have been extensively addressed in the past few years, and we thus refer the reader to the existing literature[42, 44]. The nano-fabrication was performed following these steps (Figure 1):

1) Starting from a 125 nm thick silicon on insulator wafer (UT-SOI) atop 2 μm buried oxide (BOX), we progressively thinned the UT-SOI via thermal oxidation in a rapid thermal processor leaving at the end of the process a 20 nm Si layer atop the BOX. The thermal oxide formed on the UT-SOI was removed via chemical etching in HF solution.

2) By patterning the UT-SOI via low-resolution ($\sim$2 μm) photolithography and plasma etching, we formed μm sized, UT-SOI patches (Figure 1 a) top panel). We produced square patches with sides ranging from 700 nm to 1400 nm.

3) Solid-state dewetting of the UT-SOI patches was induced by high-temperature annealing in the ultra-high vacuum (static vacuum $\sim 10^{-10}$ torr) of a molecular beam epitaxy reactor (Figure 1 a), bottom panel). Scanning electron microscopy (SEM) images confirm the formation of the Si islands on the BOX (Figure 1, b) and c)). The investigated samples host arrays of resonators spaced a few microns from each other [42, 44]. Different spacing corresponds to different average island size. Thus, on each sample we investigate arrays of nominally identical resonators extending over about 50 μm $\times$ 50 μm, having bases and heights ranging between $\sim$280 nm to $\sim$770 nm and $\sim$80 nm to $\sim$200 nm respectively. Fluctuation in resonator size is less than 10%. For an extensive characterization of SEM images of a similar sample obtained in the same dewetting conditions we refer the reader to reference [42]. These islands are monocrystalline and atomically smooth, featuring the typical facets of the equilibrium shape of silicon (113, 111 and 001), as highlighted on the atomic force microscope (AFM) height profile shown in Figure 1 b) and c). Further information on the dewetting method and Si islands features can be found in references[39, 45, 41]. From the SEM images and AFM profile, a square patch surrounding

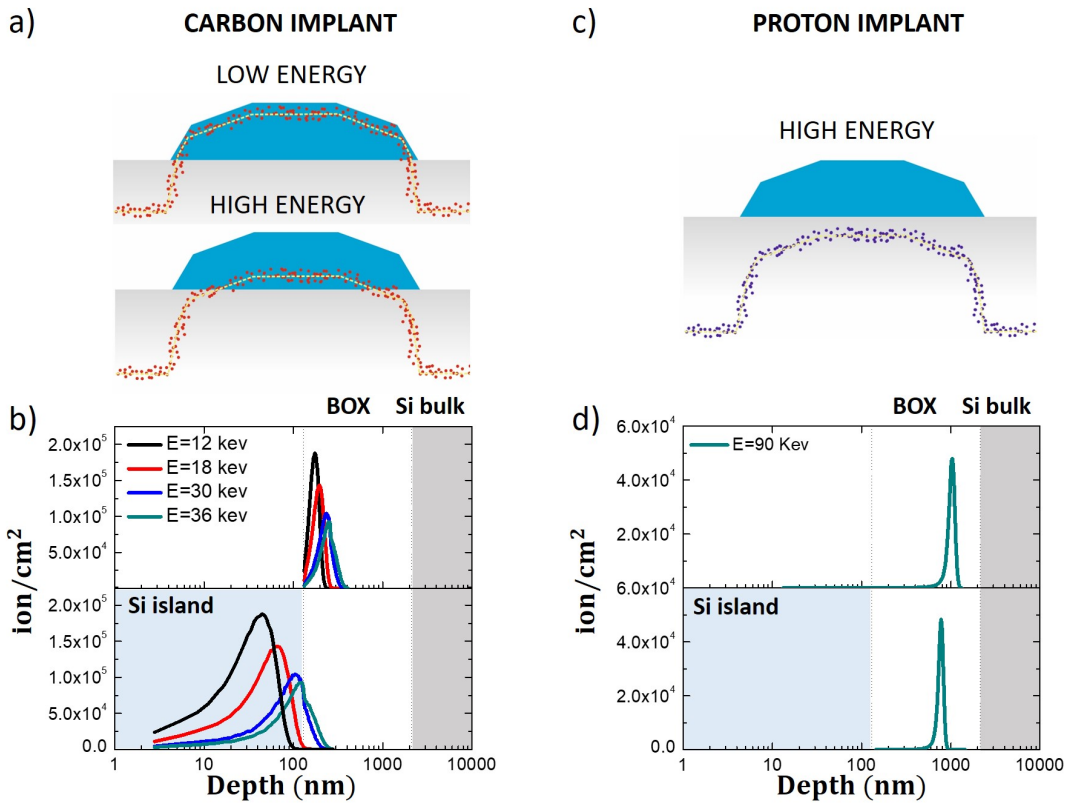

FIGURE 2 a) Scheme of the carbon implant in a Si island for low energy beam (top panel) and high energy beam (bottom panel). The ion implant was followed by a re-crystallization step via rapid thermal annealing (not shown). b) SRIM simulation of carbon implant for different beam energy in a 130 nm height Si-island (bottom panel) and in the buried oxide next to an island (BOX, top panel). c) Scheme of proton implant. d) SRIM simulation of proton implant at 90 keV through a 130 nm height Si island (bottom panel) and in the BOX, next to a Si island (top panel).

the Si islands is also visible . This is the result of a slight over-etch of the UT-SOI during the plasma etching step producing a SiO_2 pedestal. This feature (about 20 nm height) does not significantly modify the optical properties of the islands [42, 44].

4) After island formation carbon ions are implanted using various beam energies. By changing the energy of the implant we set different depths beneath the surface of the resonators at which G-centres will form (third and fourth panel of Figure 2 a)). For a fixed C dose of 10^{14} Ions/cm^2, we set the implant energy to 12, 18, 30 and 36 keV to go deeper inside the resonators. Figure 2 b), shows the corresponding implantation profiles (obtained with Montecarlo simulation using SRIM Software) at the center of a resonator (depths beneath the surface of the island at which G-centres will form, corresponding to the point of its maximal height). Given the uneven shape of the resonators, the corresponding implantation profile will be affected accordingly: the ions will stop at a different depth depending on the distance from the resonator center. This uneven implant profile will be considered in FDTD simulations to better model the light extraction phenomenon. We also took care to not implant the C ions in the bulk silicon below the BOX: irrespective of the C ions energy, the corresponding implant distribution outside a Si resonator (Figure

2 b)), is well confined within the 2μm thick BOX (in which no G-centres will be formed). Following a standard fabrication process for G-centers used in bulk and SOI[46, 24], our sample underwent a rapid thermal annealing step at 1000^{o}C under N_2 atmosphere for 20 s to repair the lattice damage that occurred during the carbon implant and incorporate C on substitutional lattice sites (not shown).

5) As a last step, in order to induce the interstitial Si that forms the G-center, the dewetted resonators underwent a proton irradiation step carried out at a beam energy of 90 keV with doses ranging from 6×10^{13} Ions/cm^2 up to 3×10^{15} Ions/cm^2 to activate the G-center emission (Figure 2 c)). The expected implant profile shows that, with and without the presence of a Si-island (Figure 2 d)), the protons stop always in the BOX. Thus, the G-centers are created only in the resonators (and not in the bulk Si, underneath the BOX) and the protons do not create unwanted defects around them as further confirmed by spectroscopy measurements as shown hereafter.

Upon dewetting and functionalization with G-centers, we do not observe any significant modification of the Si-based islands, which remain perfectly stable. Photoluminescence experiments can be conducted on the same sample many months apart. This is a further confirmation of the stability of these emitters that are robust against blinking, bleaching and thermal cycles[28, 29].

2.2 | Photoluminescence characterisation

In this section we address the experimental findings of the optimal fabrication parameters.

Figure 3 displays macro-photoluminescence spectra collected from an area outside the resonant antennas arrays and from the brightest emitting antennas array. This analysis points out that we observe the typical spectrum of G-centers only from the areas of the sample covered by antennas, as expected from the SRIM simulations (Figure 2 b)-d)) accounting for a selective G-center activation. In the spectrum we distinguish the contribution of G-centers with the ZPL at 1278 nm and its phonon side-band, featuring the typical peak of the transverse acoustic contribution at the X points of the Brillouin zone (TA(X)) and the so-called E-line attributed to a local vibrational mode of the carbon atoms, as labelled in the spectrum of Figure 3 [24].

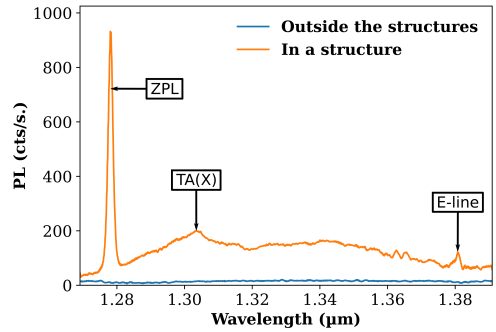

FIGURE 3 G-center spectrum. Comparison of the PL spectra collected at 12 K with an excitation by a laser diode emitting at 532 nm outside the islands array (blue curve) and for the brightest emitting islands array (orange curve).

We then study the influence of the proton dose on the photoluminescence intensity in order to find the best compromise between number of activated G-centers and creation of non-radiative defects. For all the investigated island sizes we observe an increase in the intensity of the PL with the proton dose up to an optimal value of 3×10^{14} Ions/cm^2 beyond which the intensity decreases (Figure 4 a)). See also the Supplementary Information Figure S2, where the full characterisation is displayed. This result is comparable to that previously obtained by Berhanuddin et al. with G-centers in bulk Si [47].

The previous analysis of macro-photoluminescence on islands arrays also provides information on the best resonator size and implantation energy (that is, C depth). To this end, we investigated arrays of islands irradiated with the same C dose but having different base size and using different carbon beam energy. We observe that the most intense signal was detected from the array of resonators with an average base of 507 nm and with carbon implanted with an energy of 30 keV, i.e. an average depth of implantation at 115 nm (Figure 2 b)). These results are shown in Figure 4 b), where we compare the spectra of islands with same base size, proton implant and carbon dose but implanted at 8 and 30 keV carbon beam energy determining an emission from a depth of about 42 and 115 nm, respectively.

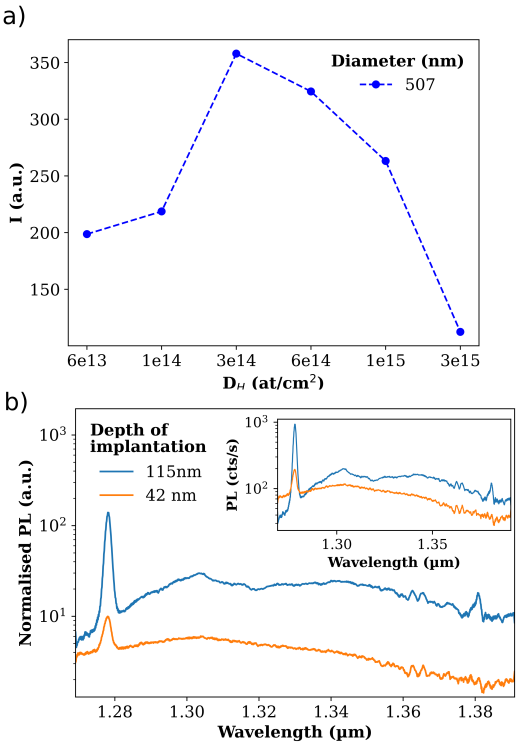

FIGURE 4 Macro photoluminescence. All the spectra were measured at 12 K with an excitation by a laser diode at 532 nm. a) Intensity of the ZPL as a function of the proton dose for resonators having a mean base diameter of 507 nm and implanted with carbon at 30 keV. c) Comparison of PL spectra for two resonators arrays having a mean base diameter of 507 nm and irradiated with the same proton dose of $3{\times}10^{14}$ Ions/cm^2, for C energy of 12 keV (orange line) and 30keV (blue line), corresponding to mean implantation depths of 42 nm and 115 nm, respectively. The intensity of the spectra are corrected considering the implant profile in the resonator (black lines) that accounts for a different number of embedded emitters. The inset shows the raw spectra before the normalization.

2.3 | Numerical optimization of the fabrication parameters

We now address the expected optical properties of the Mie resonators by considering a simplified 3D model of the resonator shape and placing individual dipole emitters within it.

In order to identify the optimal size of the Si islands to obtain Mie resonances near the wavelength of the ZPL of G-centers we carried out finite-difference time-domain (FDTD) simulations, studying the scattering cross-section under plane wave illumination at normal incidence from free space, as a function of the base diameter of the resonators (Figure 5 a)). We identified a broad resonance corresponding to the electric dipole mode (Figures 5 c) and d)) covering the wavelength of interest for G-center emission for diameters between 500 nm and 680 nm.

The low quality factor of lower order modes in Mie resonators (e.g. about 10 for electric and magnetic dipolar modes) is not suitable for the enhancement of the spontaneous emission rate of G-centers [48, 5] by promoting the so-called Purcell effect. However, using the reciprocity principle [49], we concluded that this mode is the one which can couple with free space. Therefore, the emitted power to free space of an electric dipole embedded into the resonator is maximised when the dipole is placed at a maximum of the local electric field intensity (i.e. in a so-called field "hot spot"). We confirmed this phenomenon by computing the emitted power in free space (P_{front}) for electric dipoles emitting at the wavelength of the ZPL of G-center and placed on the axis of symmetry of the resonator at different depths. Figures 5 c) and d) highlight the concordance between P_{front} and the resonance mode as expected by the reciprocity principle.

This method only gives us information on the power emitted into free space. However, what really matters to maximize the collection of the photoluminescence of a quantum emitter with conventional optics (e.g. a low NA objective lens), is to favor an upward directional scattering compared to the emission towards the underlying substrate. Therefore we also computed the extraction efficiency $\eta = \frac{P_{front}}{P_{tot}}$ depending on the depth of the dipole in the resonator. Figure 5 b) shows that the extraction efficiency increases with the depth of the dipole into the resonator which means that it is preferable to work with G-centers implanted deeper in the structure. Thus, in optimal conditions of resonator size and position of the emitter, the collection efficiency largely exceed what could be expected from bulk Si or flat SOI, where only a few % of light is out-coupled into free-space and redistributed over the half solid-angle.

Our work compares favourably with the literature, thanks

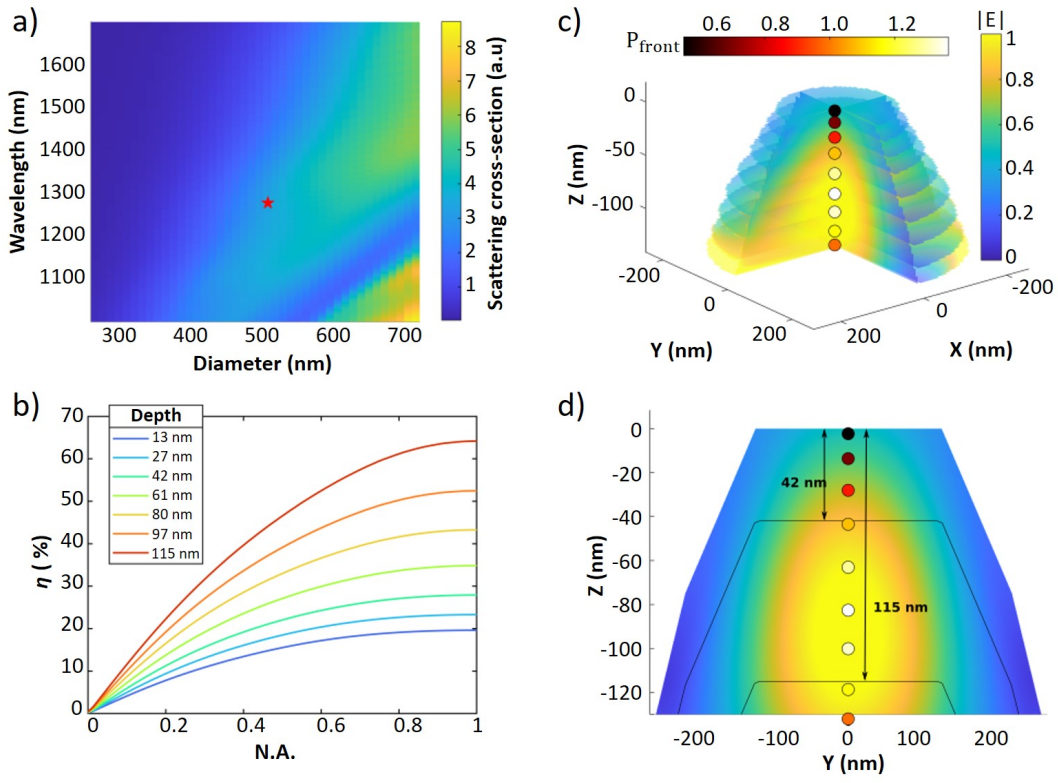

FIGURE 5 FDTD simulation. a) Total scattering cross-section of a resonator for different base diameters under plane wave illumination from the top, taking into account the presence of the BOX and the substrate. b) Computed extraction efficiency as a function of the numerical aperture (NA) of the collection optics for a dipole placed on the axis of symmetry of a resonator at different depths. c, d) 3D and 2D view of the internal electric field resulting from the excitation of the electric dipole mode at 1278 nm for a resonator having a base diameter of 507 nm. The colored spots represent the total power emitted in free space by electric dipoles emitting at 1278 nm and placed at the location of the spots. The black line (d) shows a 2D cut of the theoretical surface where G-centers are located in the resonator.

in part to the aforementioned advantages of placing the photon emitters within the bulk of the resonant antenna structures. We report the collection of 89% of photons emitted into the upper half space with an optical collection system of numerical aperture (NA) = 0.65, and 55% of the total number of photons emitted from the defect centres (η). We can compare this result with vertically standing semiconductor photonic nanowires which are well adapted to reach high collection efficiencies and to broadband operations. A collection efficiency of 43% was experimentally observed for a single quantum dot embedded in nanowire standing on a semiconductor substrate [50] and an efficiency of 72% was reported for a nanowire standing on a metallic substrate to reflect downward-emitted photons [51]. Our approach, relaxes the need for complex epitaxial fabrication and etching steps and allows, in principle, comparable performances. Similar systems are the so-called "photonic trumpet" structures (inverted cone shapes, presented in ref. [52]) which provide adiabatic expansion of a guided mode fed by photons from InAs quantum dot situated at their base, yielding vertical emission info free space. Such structures channel 95% of photons from the point emitter into the wanted guided mode, and then 59% of these photons to

free space, yielding an overall extraction efficiency of 56%. Our system therefore delivers comparable performances with a far simpler and more robust photonic structure.

More similar structures to those presented in this paper, namely silicon nanodisks embedded with SiGe quantum dots[19], demonstrate Purcell enhancement factors of around 1.5 but do not distinguish between the enhanced emission rate of photons into the disks themselves (due to a reinforced optical density of states) and collection optimisation in free space due to directional control of emitted photons.

Advanced epitaxial growth and nano-fabrication methods can be used to embed light emitters in Fabry-Perot micropillars and photonic crystal nano-cavities offering a large enhancement of the radiative spontaneous emission rate and a shaping of the emission in the far-field[53]. In these cases collection efficiencies (expressed as the collection efficiency at the first lens, that is the same figure of merit that we use) ranging between 20 to 80% can be obtained. These values are comparable to our findings that are obtained with a much simpler device and fabrication methods.

When the emitters are not embedded within the resonant antennas the collection enhancement is usually more limited. In the case of perovskite nanocrystals coupled to TiO_2-based Mie resonators, the PL enhancement reached a value of 5 with respect to bare emitters[54]. This enhancement is not far from what was previously reported by dispersing colloidal quantum dots atop Si-based Mie resonators[7]. This latter analysis clearly points out the importance of embedding the emitters within the resonant cavities when targeting a large brightness of the sources (e.g. as for quantum optics applications).

The optimal size of the resonator obtained by experimental measurements is consistent with the results of the simulations since it is in the range in which we find the resonance (see the red star on Figure 5 a)) corresponding to the electric dipole mode (Figure 5 c) and d)). We notice that we do not obtain the diameter for which the simulation predicts the strongest resonance at 1278 nm. This difference can be explained by the approximations made in the simulations for which we considered an ideal shape of resonator, that is two stacked truncated cones, and we set an average height for the resonators. Moreover, the simulations do not take into account fluctuations of shape and height of the dewetted particles within a same array [55, 42].

The optimal carbon implantation energy obtained experimentally (Figure 4 b)), which corresponds to a deep implantation, is in agreement with the simulated results: a deeper implantation results in a larger extraction of light (Fig. 5 b)). However, if we assume that the G-centers are mainly created on a surface conformal to that of the resonator and at a depth corresponding to the average depth of implanted carbon (black lines in Figure 5 d)), the probability of creating G-centers in a hot spot of the mode, and at the same time of coupling it with this mode, is increased for higher implantation depths. This explains why, at a fixed resonator size and proton dose, we obtain a more intense PL signal for the sample in which the carbon ions have been implanted at an average depth of 115 nm than that for which it is at 42 nm (inset of Figure 4 b)). Moreover, we see in Figure 5 d) that the theoretical surface in which the G-centers are mainly created is larger for a shallower implantation. This means that it is possible to create more emitters for shallower implantation. This implies that we obtain a brighter signal with a lower number of emitters, which shows the interest of placing the G-centers in the hot spot of the modes. Figure 4 b) shows the PL signal normalized by the theoretical effective surface over which G-centers are created for carbon implantation depths of 42 nm and 115 nm (black lines in Figure 5 d). This accounts for the different number of emitting defects considering that the density of G-centers is constant for the two samples given that they were implanted with the same carbon dose. This demonstrates the importance of controlling the placement of the emitters since we observe a difference in PL per unit of effective emission surface, in other words, per number of emitters, of more than one order of magnitude.

2.3.1 | Angle-resolved photoluminescence spectroscopy

We now address the far-field emission pattern of the G-centers when embedded in the resonant antennas. As the experimental setup used for angle-resolved photoluminescence does not allow us to reach temperatures below 120 K, we have focused our study on the brightest array of resonators previously identified so as to have sufficient signal. Figure 6 a) shows the spectrum of angle-resolved photoluminescence obtained at 120 K on which we observe the red-shift and the broadening

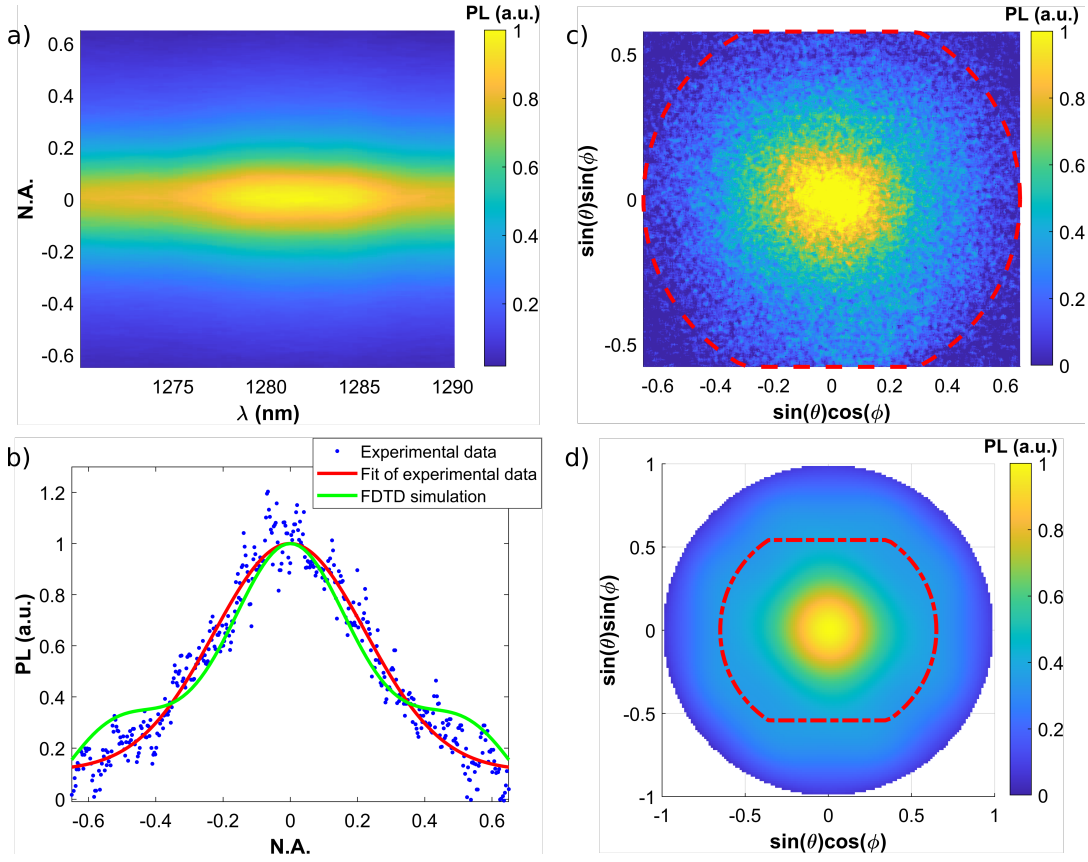

FIGURE 6 Angle-resolved spectroscopy. All the measurements have been carried out on the brightest structure at 120 K with an excitation by a laser at 532 nm. a) Angle-resolved photoluminescence pseudo-colour maps in linear scale. b) 2D cut along the $\sin(\phi) = 0$ direction of the far-field emission profile. The blue dots are the experimental data which are fitted by a Gaussian profile (red line) and the green line corresponds to the result obtain by FDTD simulation. c) Experimental and d) simulated normalized far-field emission profiles.

of the ZPL of the G-centers caused by the relatively high temperature [24]. However, we can see that we get enough signal to distinguish the emission from the G-centers, which allowed us to study their far-field emission profile, shown in Figure 6 c), using Fourier spectroscopy (see Experimental Section). In order to only collect the emission from the G-centers, we measured the far-field of the resonators in which the G-centers are embedded and we subtracted from it the measurement carried out on an area of SOI with no emitters.

This measurement gives access to the angular distribution of the photons emitted by the G-centers by counting the number of photons emitted for each wave vector of the reciprocal space. The latter is characterized by its components $k_x = (2\pi/\lambda)\sin(\theta)\sin(\phi)$ and $k_y = (2\pi/\lambda)\sin(\theta)\cos(\phi)$ where θ is the polar emission angle and ϕ is the azimuth angle. The distribution obtained experimentally can be fitted by a Gaussian profile as shown by the 2D cut for $\sin(\phi) = 0$ in Figure 6 b) where the blue points represent the experimental data and the red line the Gaussian fit. Using this fit, we can estimate the transmission efficiency of the emission in the free space to an optical collection system of numerical aperture NA defined as $T(NA) = \frac{\int_0^{NA} G(x)dx}{\int_0^1 G(x)dx}$, where G(x) is the function given by the Gaussian fit. Thus, we estimate that for the microscope objective NA = 0.65 used for this experiment

we collected 89% of the photons emitted into free space, and we can expect up to 93% of collection efficiency with NA = 0.8. These results show that the coupling of the G-centers with the resonant antennas leads to a strong directionality of the emission in the upwards direction, and so maximizes the collection efficiency during transmission to optics with standard numerical apertures.

Further insight into the underlying phenomenology is obtained by representing the electric field intensity distribution obtained by FDTD simulation for the emission of a dipole positioned on the axis of symmetry of a Mie resonator at 115 nm from the top surface (optimal conditions of resonator size and dipole position). This analysis is reported in the Supplementary Information Figure S3 and clearly shows a much larger intensity of the electric field in the upwards direction with respect to the intensity radiated into the underlying substrate. To confirm the directionality of the emission we also reported the Poynting vector (as arrows) showing that the dipole emits more power into free space than into the BOX and that a large part of the power emitted into free space can be collected with conventional optics.

The experimental results are compared with the predictions obtained by FDTD with a dipole placed on the axis of symmetry of the resonator at a depth of 115 nm (Figure 6 b) and d)). For numerical apertures lower than 0.35, the far-field profile predicted by this simulation is close to the Gaussian profile which fits the experimental data. On the other hand, for NA > 0.35 a small plateau appears in the simulated far-field profile that we cannot distinguish experimentally. This discrepancy between the simulation and the experimental results can have several origins, the first being the fluctuation of size and shape of the resonators in an array as explained previously. Another explanation is that we consider only one emitter in our simulation whereas there can be several in a single Si resonator at slightly different depths. Therefore our simulations do not take into account the collective effects of the various emitters as well as their distribution in the resonator. Consequently it is not possible to obtain an absolute quantitative prediction from the simulations. However, the similarities between the experimental and computed results allow us to qualitatively estimate the influence of the parameters such as the size of the resonator and the location of the emitters on the emission which results from the coupling between the two. In particular, the deeper the emitters are in the resonators, the larger the extraction efficiency (Figure 5 b)). This, added to the high directionality of the emission, allows us to improve the ratio of collected photons with respect to the total emission of a G-center (e.g. compared to what is obtained in flat SOI, without a photonic structure).

2.4 | Conclusion

In conclusion, we showed for the first time Si-based submicrometric Mie resonators embedding quantum emitters featuring a bright and directional photoluminescence at near-infrared frequencies. Exploiting the dewetting instability of thin films, a hybrid top-down/bottom-up nano-fabrication method, we can form small resonators with low-resolution, optical lithographic methods. These antennas, unlike Si-based Mie resonators obtained via conventional top-down nano-fabrication approaches, are monocrystalline and defect free, with atomically smooth facets, thus limiting the defects at the air-Si interfaces. Engineering the implant profile of C ions and proton fluency, we can obtain light-emitting antennas featuring a high extraction efficiency, channeling up to 89% of the light towards a conventional objective lens, as verified by FDTD simulations. These results are important in view of the creation of individual emitters in Si-based nano-antennas, relaxing the need for complex photonic devices (e.g. photonic crystals, Fabry-Perot microcavities) and for applications in quantum optics, such as quantum cryptography and quantum computation.

2.5 | Experimental Section

Measurement procedures: Macro-photoluminescence measurements were performed at 12 K cooling the sample with a closed-cycle liquid-helium cryostat. The optical pumping was performed with a continuous wave (cw) laser diode at 532 nm focused onto the sample with a lens offering a focus spot of ≈ 75 µm. The PL emission was collected by a Cassegrain objective which collects light between 0.15 to 0.4 numerical aperture (NA) and focused on an optical fiber connected to a spectrometer coupled with a liquid nitrogen-cooled InGaAs detector enabling spectral detection from 900 to 1600 nm. For the angle-resolved photoluminescence spectroscopy the

samples were cooled down to approximately 120 K with a liquid-nitrogen cryostat. The optical pumping was performed with a cw laser diode at 532 nm focused with a microscope objective (×50, NA = 0.65). The PL signal was collected through the same objective and filtered by a band-pass filter within 1250-1300 nm. The output signal was projected onto the entrance of a spectrometer coupled to an InGaAs CMOS camera (NIRVANA Princeton).

Simulation : The FDTD simulations were performed with the commercial software Ansys Lumerical Simulation. The refractive index of Silicon and Silica where taken from the materials database of the software. The simulation area was delimited by perfectly matched layer (PML) boundaries. The scattering cross-sections have been obtained using a cross section box placed outside a TFSF source. The representations of the electric dipole mode have been obtained by placing several monitors in the resonator. Two other monitors have been placed above and beneath the resonator to obtain the emitted power in the two directions as well as the far-field data.

ACKNOWLEDGEMENTS

The authors thank the Nanotecmat platform of the IM2NP institute. We acknowledge V. Jacques, G. Cassabois, A. Dréau, and J.-M. Gérard for the useful discussion.

CONFLICT OF INTEREST

The authors declare no conflict of interest

REFERENCES

[1] Dong P, Chen YK, Duan GH, Neilson DT. Silicon photonic devices and integrated circuits. Nanophotonics 2014;3(4-5):215–228.

[2] Bernabe S, Wilmart Q, Hasharoni K, Hassan K, Thonnart Y, Tissier P, et al. Silicon photonics for terabit/s communication in data centers and exascale computers. Solid-State Electronics 2021;179:107928.

[3] Kuznetsov AI, Miroshnichenko AE, Brongersma ML, Kivshar YS, Luk'yanchuk B. Optically resonant dielectric nanostructures. Science 2016;354(6314).

[4] Sain B, Meier C, Zentgraf T. Nonlinear optics in all-dielectric nanoantennas and metasurfaces: a review. Advanced Photonics 2019;1(2):024002.

[5] Liu J, Shi M, Chen Z, Wang S, Wang Z, Zhu S, Quantum photonics based on metasurfaces; 2021. http://www.chinaoceanengin.cn//article/id/6065740399d8817cffa1aa5c.

[6] Bidault S, Mivelle M, Bonod N. Dielectric nanoantennas to manipulate solid-state light emission. Journal of Applied Physics 2019;126(9):094104.

[7] Staude I, Khardikov VV, Fofang NT, Liu S, Decker M, Neshev DN, et al. Shaping photoluminescence spectra with magnetoelectric resonances in all-dielectric nanoparticles. ACS Photonics 2015;2(2):172–177.

[8] Zhou B, Liu M, Wen Y, Li Y, Chen R, Atomic layer deposition for quantum dots based devices; 2020. http://www.chinaoceanengin.cn//article/id/5fa4dc9ff4d7917194c90a84.

[9] Todisco F, Malureanu R, Wolff C, Gonçalves P, Roberts AS, Mortensen NA, et al. Magnetic and electric Mie-exciton polaritons in silicon nanodisks. Nanophotonics 2020;9(4):803–814.

[10] Lepeshov S, Wang M, Krasnok A, Kotov O, Zhang T, Liu H, et al. Tunable resonance coupling in single Si nanoparticle–monolayer WS2 structures. ACS applied materials & interfaces 2018;10(19):16690–16697.

[11] Cihan AF, Curto AG, Raza S, Kik PG, Brongersma ML. Silicon Mie resonators for highly directional light emission from monolayer MoS 2. Nature Photonics 2018;12(5):284–290.

[12] Bucher T, Vaskin A, Mupparapu R, Lochner FJ, George A, Chong KE, et al. Tailoring photoluminescence from MoS2 monolayers by Mie-resonant metasurfaces. ACS Photonics 2019;6(4):1002–1009.

[13] Kerker M, Wang DS, Giles C. Electromagnetic scattering by magnetic spheres. JOSA 1983;73(6):765–767.

[14] Decker M, Staude I, Falkner M, Dominguez J, Neshev DN, Brener I, et al. High-efficiency dielectric Huygens' surfaces. Advanced Optical Materials 2015;3(6):813–820.

[15] Babicheva VE, Evlyukhin AB. Resonant lattice Kerker effect in metasurfaces with electric and magnetic optical responses. Laser & Photonics Reviews 2017;11(6):1700132.

[16] Shamkhi HK, Baryshnikova KV, Sayanskiy A, Kapitanova P, Terekhov PD, Belov P, et al. Transverse scattering and generalized kerker effects in all-dielectric mie-resonant metaoptics. Physical review letters 2019;122(19):193905.

[17] Choi B, Iwanaga M, Sugimoto Y, Sakoda K, Miyazaki HT. Selective plasmonic enhancement of electric-and magnetic-dipole radiations of Er ions. Nano letters 2016;16(8):5191–5196.

[18] Capretti A, Lesage A, Gregorkiewicz T. Integrating quantum dots and dielectric Mie resonators: a hierarchical metamaterial inheriting the best of both. ACS photonics 2017;4(9):2187–2196.

[19] Rutckaia V, Heyroth F, Novikov A, Shaleev M, Petrov M, Schilling J. Quantum dot emission driven by Mie resonances in silicon nanostructures. Nano letters 2017;17(11):6886–6892.

[20] Yuan S, Qiu X, Cui C, Zhu L, Wang Y, Li Y, et al. Strong photoluminescence enhancement in all-dielectric Fano metasurface with high quality factor. ACS nano 2017;11(11):10704–10711.

[21] Davies G. The optical properties of luminescence centres in silicon. Physics reports 1989;176(3-4):83–188.

[22] Davies G, Hayama S, Murin L, Krause-Rehberg R, Bondarenko V, Sengupta A, et al. Radiation damage in silicon exposed to high-energy protons. Physical Review B 2006;73(16):165202.

[23] Chartrand C, Bergeron L, Morse K, Riemann H, Abrosimov N, Becker P, et al. Highly enriched Si 28 reveals remarkable optical linewidths and fine structure for well-known damage centers. Physical Review B 2018;98(19):195201.

[24] Beaufils C, Redjem W, Rousseau E, Jacques V, Kuznetsov AY, Raynaud C, et al. Optical properties of an ensemble of G-centers in silicon. Physical Review B 2018;97(3):035303.

[25] Khoury M, Abbarchi M. A bright future for silicon in quantum technologies. Journal of Applied Physics 2022;131(20):200901. https://doi.org/10.1063/5.0093822.

[26] Hollenbach M, Berencén Y, Kentsch U, Helm M, Astakhov GV. Engineering telecom single-photon emitters in silicon for scalable quantum photonics. Optics Express 2020;28(18):26111–26121.

[27] Bergeron L, Chartrand C, Kurkjian A, Morse K, Riemann H, Abrosimov N, et al. Silicon-integrated telecommunications photon-spin interface. PRX Quantum 2020;1(2):020301.

[28] Redjem W, Durand A, Herzig T, Benali A, Pezzagna S, Meijer J, et al. Single artificial atoms in silicon emitting at telecom wavelengths. Nature Electronics 2020;3(12):738–743.

[29] Durand A, Baron Y, Redjem W, Herzig T, Benali A, Pezzagna S, et al. Broad diversity of near-infrared single-photon emitters in silicon. Physical Review Letters 2021;126(8):083602.

[30] MacQuarrie E, Chartrand C, Higginbottom D, Morse K, Karasyuk V, Roorda S, et al. Generating T centres in photonic silicon-on-insulator material by ion implantation. New Journal of Physics 2021;23(10):103008.

[31] Kurkjian A, Higginbottom D, Chartrand C, MacQuarrie E, Klein J, Lee-Hone N, et al. Optical observation of single spins in silicon. arXiv preprint arXiv:210307580 2021;.

[32] Baron Y, Durand A, Udvarhelyi P, Herzig T, Khoury M, Pezzagna S, et al. Detection of single W-centers in silicon. arXiv preprint arXiv:210804283 2021;.

[33] Udvarhelyi P, Somogyi B, Thiering G, Gali A. Identification of a telecom wavelength single photon emitter in silicon. Physical review letters 2021;127(19):196402.

[34] Bergeron L, Chartrand C, Kurkjian A, Morse K, Riemann H, Abrosimov N, et al. Characterization of the T center in 28Si. arXiv preprint arXiv:200608794 2020;.

[35] Cloutier SG, Kossyrev PA, Xu J. Optical gain and stimulated emission in periodic nanopatterned crystalline silicon. Nature materials 2005;4(12):887–891.

[36] Zhu L, Yuan S, Zeng C, Xia J. Manipulating Photoluminescence of Carbon G-center in Silicon Metasurface with Optical Bound States in the Continuum. Advanced Optical Materials 2020;8(8):1901830.

[37] Tian F, Sumikura H, Kuramochi E, Takiguchi M, Ono M, Shinya A, et al. All-optical dynamic modulation of spontaneous emission rate in hybrid optomechanical emitter-cavity systems. Optica 2022;9(3):309–316.

[38] Prabhu M, Errando-Herranz C, De Santis L, Christen I, Chen C, Englund DR. Individually Addressable Artificial Atoms in Silicon Photonics. arXiv preprint arXiv:220202342 2022;.

[39] Abbarchi M, Naffouti M, Vial B, Benkouider A, Lermusiaux L, Favre L, et al. Wafer Scale Formation of Monocrystalline Silicon-Based Mie Resonators via Silicon-on-Insulator Dewetting. ACS Nano 2014;8(11):11181–11190.

[40] Naffouti M, Backofen R, Salvalaglio M, Bottein T, Lodari M, Voigt A, et al. Complex dewetting scenarios of ultrathin silicon films for large-scale nanoarchitectures. Science Advances 2017 nov;3(11).

[41] Bollani M, Salvalaglio M, Benali A, Bouabdellaoui M, Naffouti M, Lodari M, et al. Templated dewetting of single-crystal sub-millimeter-long nanowires and on-chip silicon circuits. Nat Commun 2019 dec;10(1):5632.

[42] Toliopoulos D, Khoury M, Bouabdellaoui M, Granchi N, Claude JB, Benali A, et al. Fabrication of spectrally sharp Si-based dielectric resonators: combining etaloning with Mie resonances. Optics Express 2020 dec;28(25):37734.

[43] Benali A, Claude JB, Granchi N, Checcucci S, Bouabdellaoui M, Zazoui M, et al. Flexible photonic devices based on dielectric antennas. Journal of Physics: Photonics 2020;2(1):015002.

[44] Granchi N, Montanari M, Ristori A, Khoury M, Bouabdellaoui M, Barri C, et al. Near-field hyper-spectral imaging of resonant Mie modes in a dielectric island. APL Photonics 2021 dec;6(12):126102.

[45] Naffouti M, Backofen R, Salvalaglio M, Bottein T, Lodari M, Voigt A, et al. Complex dewetting scenarios of ultrathin silicon films for large-scale nanoarchitectures. Sci Adv 2017;3(11):eaao1472.

[46] Berhanuddin DD, Lourenço MA, Gwilliam RM, Homewood KP. Co-Implantation of Carbon and Protons: An Integrated Silicon Device Technology Compatible Method to Generate the Lasing G-Center. Advanced Functional Materials 2012 apr;22(13):2709–2712.

[47] Berhanuddin DD, Lourenço MA, Gwilliam RM, Homewood KP. Co-Implantation of Carbon and Protons: An Integrated Silicon Device Technology Compatible Method to Generate the Lasing G-Center. Advanced Functional Materials 2012;22(13):2709–2712. _eprint: https://onlinelibrary.wiley.com/doi/pdf/10.1002/adfm.201103034.

[48] Rutckaia V, Heyroth F, Novikov A, Shaleev M, Petrov M, Schilling J. Quantum Dot Emission Driven by Mie Resonances in Silicon Nanostructures. Nano Letters 2017 Nov;17(11):6886–6892.

[49] Vaskin A, Kolkowski R, Koenderink AF, Staude I. Light-emitting metasurfaces. Nanophotonics 2019 Jul;8(7):1151–1198. Publisher: De Gruyter.

[50] Reimer ME, Bulgarini G, Fognini A, Heeres RW, Witek BJ, Versteegh MAM, et al. Overcoming power broadening of the quantum dot emission in a pure wurtzite nanowire. Physical Review B 2016;93(19):195316.

[51] Claudon J, Bleuse J, Malik NS, Bazin M, Jaffrennou P, Gregersen N, et al. A highly efficient single-photon source based on a quantum dot in a photonic nanowire. Nature Photonics 2010;4(3):174.

[52] Stepanov P, Delga A, Gregersen N, Peinke E, Munsch M, Teissier J, et al. Highly directive and Gaussian far-field emission from “giant” photonic trumpets. Applied Physics Letters 2015;107(14):141106.

[53] Senellart P, Solomon G, White A. High-performance semiconductor quantum-dot single-photon sources. Nature nanotechnology 2017;12(11):1026–1039.

[54] Suárez I, Wood T, Pastor JPM, Balestri D, Checcucci S, David T, et al. Enhanced nanoscopy of individual CsPbBr3 perovskite nanocrystals using dielectric sub-micrometric antennas. APL Materials 2020;8(2):021109.

[55] Abbarchi M, Naffouti M, Lodari M, Salvalaglio M, Backofen R, Bottein T, et al. Solid-state dewetting of single-crystal silicon on insulator: effect of annealing temperature and patch size. Microelectronic Engineering 2018;190:1–6.